RapidScat SIR-Enhanced Scatterometer *EASE-Grid 2.0* Radar Backscatter NSIDC-0809

Algorithm Theoretical Basis Document
Version 1
April 7, 2026

David G. Long[1], Julie Z. Miller[2,3]

[1] *Microwave Earth Remote Sensing Laboratory, Brigham Young University, Provo, UT, USA*

[2] *EarthSAR, LLC, Salt Lake City, UT, USA*

[3] *Earth Science and Observation Center, Cooperative Institute for Research in Environmental Sciences, University of Colorado, Boulder, CO, USA*

Cover Image
Color montage of morning overpass AMSR2 horizontally-polarized 36 GHz passive microwave brightness temperatures, 29–30 June, 2003, by M. J. Brodzik, National Snow and Ice Data Center.

Citation
David G. Long & Julie Z. Miller. 2026. RapidScat SIR-Enhanced Scatterometer EASE-Grid 2.0 Radar Backscatter Algorithm Theoretical Basis Document, Version 1.
NSIDC White Paper. https://doi.org/10.5281/zenodo.19219903.

Contents

List of Figures

List of Tables

1 Revision History

Table 1: *ATBD Revision History*

Revision	Date	Purpose
1.0	2026-04-07	Initial Version

Table 2: *Data Set Revision History*

Revision	Date	Purpose
1.0	2026-04-07	Initial Data Release

2 Acronyms and Abbreviations

Table 3: *List of Acronyms and Abbreviations*

ADEOS	Advanced Earth Observing Satellite
ATBD	Algorithm Theoretical Basis Document
AVE	weighted AVEraging image formation algorithm
BYU	Brigham Young University
CETB	Calibrated Passive Microwave Daily EASE-Grid 2.0 Brightness Temperature
CF	Climate and Forecast Metadata Conventions
DAAC	Distributed Active Archive Center
dB	decibel ($10\log_{10}$)
DIB	Drop-In-the-Bucket averaging (used to produce GRD products)
DOY	Day Of Year
E2T	EASE-Grid 2.0, Temperate and Tropical Cylindrical Projection
EASE-Grid	Equal-Area Scalable Earth Grid (Original Definition)
EASE-Grid 2.0	Equal-Area Scalable Earth Grid Version 2.0
EASE2-M	EASE-Grid 2.0, Mid- and Low-Latitude Cylindrical Projection
EASE2-N	EASE-Grid 2.0, Northern Hemisphere Projection
EASE2-S	EASE-Grid 2.0, Southern Hemisphere Projection
EASE2-T	EASE-Grid 2.0, Temperate and Tropical Cylindrical Projection
EOSDIS	Earth Observing System Data and Information System
ESDR	Earth System Data Record
FA	incidence-angle Fixed Azimuth modulation coefficients
GHz	GigaHertz
GRD	(Drop-In-the-Bucket) Gridding Method
HH	Horizontal-polarization transmit, Horizontal-polarization receive
ISS	International Space Station
JPL	Jet Propulsion Laboratory
LTOD	local-time-of-day
MEaSUREs	Making Earth System Data Records for Use in Research Environments
NASA	National Aeronautics and Space Administration
NSCAT	NASA Scatterometer
NSIDC	National Snow and Ice Data Center
NetCDF	Network Common Data Format
PSRF	Pixel Spatial Response Function
RapidScat	RapidScat product
SCP	Scatterometer Climate Record Pathfinder
Sigma-0	normalized radar cross section or backscatter (σ^o)

SIR	Scatterometer Image Reconstruction
SRF	Spatial Response Function
UTC	Coordinated Universal Time
VV	Vertical-polarization transmit, Vertical-polarization receive

3 Purpose of this Document

This documents describes the CETB-compatible radar backscatter product "RapidScat Twice-Daily SIR-Enhanced EASE-Grid 2.0 Radar Backscatter", (NSIDC-078X, doi:TBD) created from 13.6 GHz SeaWinds Scatterometer observations collected during the RapidScat mission.

The SeaWinds scatterometer flew on two spacecraft[1]: the U.S. QuikSCAT (1999-2017) and the Japan Advanced Earth Observation System II (ADEOS2) (2003). A third SeaWinds instrument known as RapidScat flew on the International Space Station (ISS) from Sept. 2014 through Aug. 2016 (Paget et al., 2016, Durden and Perkovic-Martin, 2017, Madsen and Long, 2016). Using a scanning dual pencil-beam antenna, SeaWinds collected VV- and HH-polarized normalized radar cross section or radar backscatter (σ^o) at two incidence angles over a 1600 km wide swath (Fig. 1) at two simultaneous resolutions: eggs (footprint) at $\sim$25 km resolution and slices at $\sim 6\times 20$ km resolution (Spencer et al., 2003, Perry, 2001).

While designed and optimized for ocean wind observation, RapidScat also collected σ^o measurements over land and ice. The observed σ^o depends on the surface roughness, observation geometry, and dielectric constant. These depend on geophysical parameters of interest, such as surface freeze/thaw state, snow and ice structure, moisture content, and vegetation characteristics, among others (Ulaby and Long, 2014).

The *RapidScat* product exploits RapidScat mission (SeaWinds on the ISS) σ^o measurements to create a unique σ^o data set that captures the state of the Earth during the mission timeline. To exploit this data, we employ image reconstruction techniques to create daily and twice-daily conventional and enhanced resolution images from the σ^o measurements. The σ^o new data set is provided to the science community to support cryosphere and climate studies.

[1]By JPL convention, SeaWinds on QuikSCAT is termed 'QuikSCAT' while SeaWinds on ADEOS2 is somewhat confusingly termed 'SeaWinds' (Perry, 2001). SeaWinds on the ISS is named RapidScat.

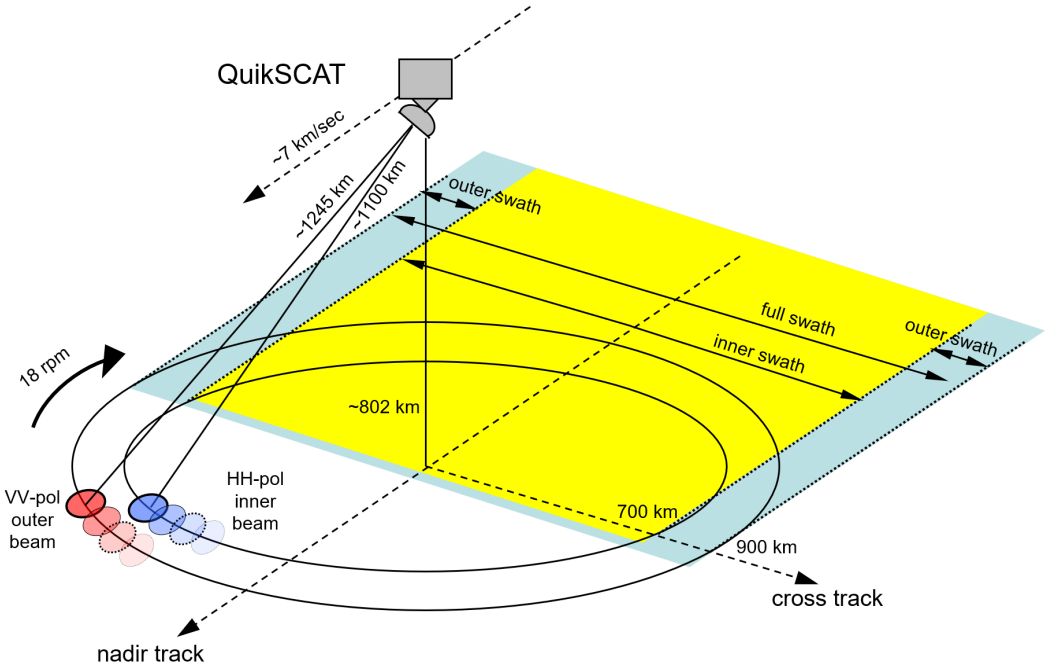

Figure 1: *Illustration of SeaWinds on QuikSCAT swath geometry. RapidScat is a similar configuration. VV-polarization σ^o measurements are collected over a 1800 km swath, with HH-polarization measurements collected over a 1400 km swath (Spencer et al., 2000, Perry, 2001, Madsen and Long, 2016).*

4 Gridded and SIR-Enhanced Product Description

4.1 Product Description

The *RapidScat* product includes Level 1 gridded radar backscatter data collected at 13.4 GHz for two radar channels (horizontal transmit-horizontal receive [HH] and vertical transmit-vertical receive [VV]. Data are gridded to the EASE-Grid 2.0 Azimuthal and Cylindrical projections (Brodzik et al., 2012, 2014), at two spatial resolutions, as described below. The *RapidScat* product is archived and distributed by the National Snow and Ice Data Center Distributed Active Archive Center (`https://doi.org/10.5067/MTQUFEXMZ3EE`).

Input data for the *RapidScat* v1.0 product is the "RapidScat Level 1B Time-Ordered Geo-Located Sigma-0 Version 2.0" (Project, 2025) in hdf4 file format from the PO.DAAC. Using the quality flags in the input data, only the highest quality measurements are included in *RapidScat* product. The product data coverage is global for the period beginning 3 Oct 2014 (DOY 276) through 19 Aug 2016 (DOY 232). The original L1B σ^o measurements are used with no additional calibration corrections applied to the data.

4.2 RapidScat Instrument Background

RapidScat was a SeaWinds instrument that flew aboard the ISS. It was spaceborne scatterometer in a *non-polar, non-sun-synchronous orbit* (Madsen and Long, 2016, Durden and Perkovic-Martin, 2017, Fore et al., 2013, Paget et al., 2016), unlike the two previous SeaWinds instruments on QuikSCAT and ADEOS-2 that flew in polar sun-synchronous orbits (Spencer et al., 2000, Perry, 2001, Spencer et al., 2003). Like SeaWinds on QuikSCAT and ADEOS-2, RapidScat collected measurements of the normalized radar cross-section (σ^o) of the Earth's surface. Over the oceans, these measurements are used to estimate the near-surface vector wind. Over the polar regions scatterometer backscatter measurements are useful for mapping melt, sea ice coverage, tracking icebergs, etc. (Long, 2017c). However, the low-inclinatiion orbit of the ISS precluded RapidScat coverage of the poles. Nevertheless, it provided frequent coverage of ice-covered region in the mid-latitudes.

Because RapidScat uses a conically scanning dual-pencil beam, the rotation of its parabolic reflector sweeps out circles on the Earth's surface centered around the nadir point of the satellite, see Fig. 1. (Technically, the pattern is a helix since the spacecraft nadir advances approximately 25 km during the antenna rotation.) There are two beams that sweep out in a conical scan, with one providing observations at approximately 46° and the other at 54.6° Earth incidence angle (EIA). Measurements from each of the two beams can be divided into two groups, forward-looking and aft-looking, defined by the antenna azimuth angle. Thus, a given point on the Earth's surface in the outer swath is observed twice by the VV-pol outer beam: once with the beam looking forward, and once with the beam looking backward. Within the inner swath, a given point is observed four times with two mea-

surements, forward-looking and aft-looking, for each of the two beams. This observation scheme is essential to providing the azimuthal diversity required for wind retrieval (Ulaby and Long, 2014).

SeaWinds collects return echo power measurements, which are converted into σ^o using the radar equation (Perry, 2001, Spencer et al., 2003, Ulaby and Long, 2014, Long, 2017a). The σ^o value depends on the surface roughness, geometry, and dielectric constant (Ulaby and Long, 2014). The measured power P_r is the integral of the surface σ^o weighted by the measurement spatial response function (SRF) as described in Sec. 5.3. The SRF is largely defined by the two-way antenna pattern. Note that while a radiometer's footprint is defined by the antenna pattern, the radar footprint is defined by the antenna pattern squared due to the two-way travel of the signal from radar to the surface (Ulaby and Long, 2014). The nominal resolution of the footprint (egg) is described as nominally 25 km, though the effective resolution varies over the antenna rotation and orbit. Signal processing of the return echo divides the footprint into finer areas known as 'slices' (Perry, 2001, Spencer et al., 2003, Long, 2017a). Figure 2 illustrates the relative SRFs for eggs and slices as a function of the antenna rotation. Figure 3 provides a zoomed-in view of the response functions.

As described below, from the σ^o measurements multiple global images are created by (1) drop-in-the-bucket (DIB) gridding of the σ^o measurements and (2) applying the SIR algorithm to enhance the effective resolution of the data by exploiting the irregular patterns of measurement locations and signal oversampling (from overlaps in adjacent footprints and overlapping swaths). The enhanced resolution SIR images are reported on a 3.125 km grid, while the DIB images are reported on a 25 km grid.

4.3 Time Division

While previous SeaWinds instruments flew in a near-polar sun-synchronous orbit at an altitude of approximately 800 km, RapidScat flew at a lower altitude in a low-inclination angle, near-tropical orbit. Sun-synchronous satellites are unique because they pass over a given point on the Earth's surface at nearly the same local time for any particular ascending or descending pass. In other words, sun-synchronous satellites maintain a constant angle to the sun, so measurements are always made at a similar local time of day. This was not the case for RapidScat for which the local time of the observation gradually changed from orbit to orbit so that eventually all local times are sampled (Paget et al., 2016).

Over a day or two period, the radar observations at a given location on the earth fall within two narrow diurnal windows. At the equator, these correspond to the ascending and descending orbit passes. Near the poles, the temporal windows widen but remain relatively narrow. Since surface temperatures can fluctuate widely during the day, simple daily averaging is problematic in the polar regions since it smears diurnal temperature fluctuations in the averaged σ^o which is very sensitive to melt conditions (Long, 2017c).

By convention, the time measurements collected on board the spacecraft are specified in UTC. The LTOD of a particular measurement at the measurement location is UTC time shifted by the longitude of location. Note that the LTOD at the prime meridian (0° longitude) is the same as the UTC time. The LTOD of locations east of the prime meridian are earlier, while locations west of the prime meridian are later. To give a specific example, consider UTC and LTOD specified in fractional hours[2]. LTOD can be computed as

$$LTOD_{\text{raw}} = UTC - longitude * 24/360 \quad (1)$$

where $longitude$ is given in degrees, typically 0° to 360° or −180° to 180°. Note that for one 24-hour UTC day, the computed $LTOD_{\text{raw}}$ values can be negative or greater than 24 hours. This has important implications discussed below. Since the computation can result in $LTOD_{\text{raw}}$ values greater than 24 or less than zero, the final LTOD value is computed modulo 24. As noted elsewhere, some geophysical processes depend on solar illumination (e.g., freeze/tha), and thus on the LTOD. Hence, knowing and properly treating the LTOD of the measurements can be important (Paget et al., 2016). Note that since the LTOD of the RapidScat observations at a given location vary with time, the *RapidScat* includes images[3] arrays of the mean LTOD and standard deviation of the LTOD of the σ^o measurements used to compute pixel values. This value is given in minutes of the day from 0 to 1440.

4.4 Grid Spatial Extent

Azimuthal *RapidScat* grids extend to the full Northern (EASE2-N) and Southern (EASE2-S) hemispheres (Fig. 4), as described in Brodzik et al. (2012, 2014). The spatial extent of the equal-area cylindrical projections (Fig. 5 and Fig. 6) is defined to match the extent of compatible grids favored by two user communities: (1) the Mid-Latitude (EASE2-M) grid, extending to ±85.0445664° latitude, has been adopted by the SMAP user community. And, (2) the Temperate and Tropical (EASE2-T) grid, limited to latitudes equatorward of ±67.1°, is consistent with the original CETB products defined for similar scanning radiometers (Brodzik et al., 2021)(Brodzik et al., 2016) and radars (Long and Miller, 2022). See Appendix A Table 6 for grid specifications.

[2]This value is multiplied by 60 to compute the LTOD in minutes.

[3]Note that LTOD is a circular value because 24:00 is the same as 00:00. This complicates compute the mean and standard deviation of LTOD values. For this product, a simplified algorithm is used. The mean and mean sum of squares (MSS) values of the LTOD and the modulo(LTOD+720,1440) at each pixel are separately computed. The mean value corresponding to the smallest MSS value is set to the mean value (after correction for the 1/2 day, 720 minute shift if required) and the corresponding standard deviation computed and recorded. This approximate approach is very accurate for the ascending-only and descending-only cases since the LTOD variance is small. For the larger variance of the both-passes case, the algorithm can select the incorrect branch.

4.5 Grid Spatial Resolution

RapidScat grid resolutions are defined relative to a 25 km base resolution, i.e., 25 km and 3.125 km MEaSUREs CETB data products (Brodzik et al., 2021). Nested resolutions relative to the CETB 25 km base grids are defined using exact divisors of 2, as illustrated in Figure 7. *RapidScat* projection extents, dimensions and grid cell size details are included in Appendix A. Grids used for *RapidScat* processing are included in Table 4.

Table 4: *RapidScat EASE-Grid 2.0 base grids produced by the GRD and SIR projection and reconstruction algorithms. See Section 5 for GRD and SIR reconstruction details.*

EASE2-M	EASE2-N	EASE2-S	EASE2-T
n/a	25km (GRD)	25km (GRD)	25km (GRD)
n/a	3.125km (GRD/SIR)	3.125km (GRD/SIR)	3.125km (GRD/SIR)

4.6 Data Products

The *RapidScat* product at the NSIDC DAAC is global and covers the period beginning 3 Oct 2014 (DOY 276) through 19 Aug 2016 (DOY 232). No calibration corrections were applied to the data. In creating a time series, a "moving average" approach was used with overlapping imaging periods that start every mission day and extend through the desired 1- or 2-day period (or to the end of the mission, whichever comes first). The 4-day images start every other day. Table 5 summarizes the available *RapidScat* products, which are all in CETB-standard EASE-2 Grid projections. Sample images visualizations are given in Figs. 11–14.

Table 5: *Available RapidScat image products (2014-2016).*

Type	days	Algorithm	Pix. Res. (km)	Regions*	Polarations	LTOD All/T	Size† T (MB)
eggs	1,2,4	GRD	25	T	HH,VV	B,A,D	3.8,3.5,3.5
eggs	1,2,4	SIR	3.125	T	HH,VV	B,A,D	190,170,170
slices	1,2,4	GRD	25	T	HH,VV	B,A,D	4.2,3.8,3.8
slices	1,2,4	SIR	3.125	T	HH,VV	B,A,D	275,230,230

∗ Region code: T=Global
† Representative uncompressed size

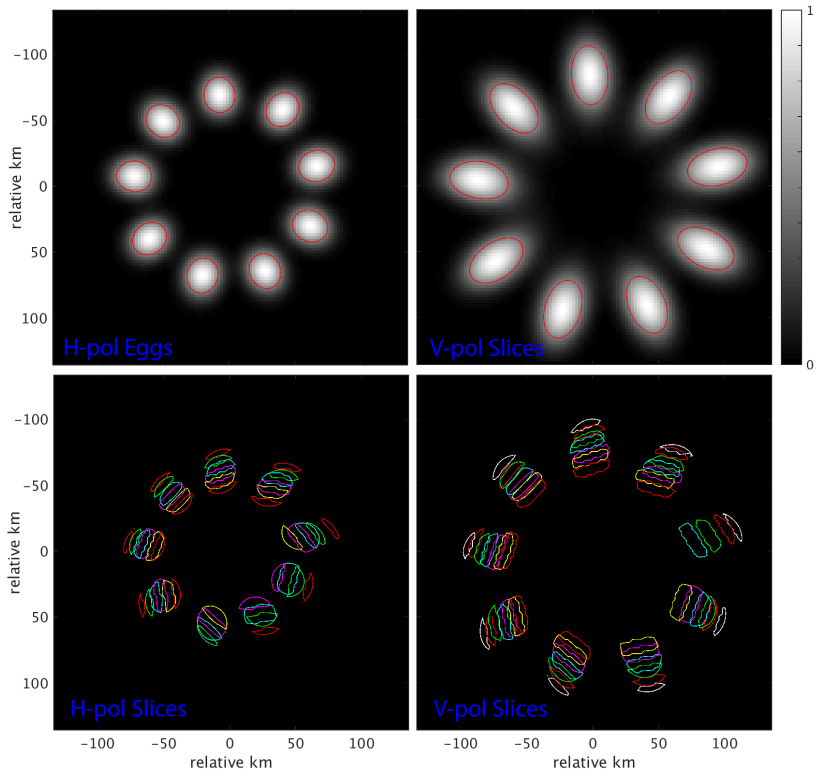

Figure 2: *Illustration of (top row) egg and (bottom row) slice SRFs and how they vary as a function of antenna rotation angle for (left column) HH-polarization (the inner-beam) and (right column) VV-polarization (the outer-beam) measurements. Contours are shown at -3 dB from the peak response. For clarity, only contours are shown for slices that often overlap. For the purposes of visualization, the plots have been horizontally shifted to appear close together whereas they are actually very far apart. Jagged edges of the slice contours are the result of the quantized grid on which the SRF is evaluated.*

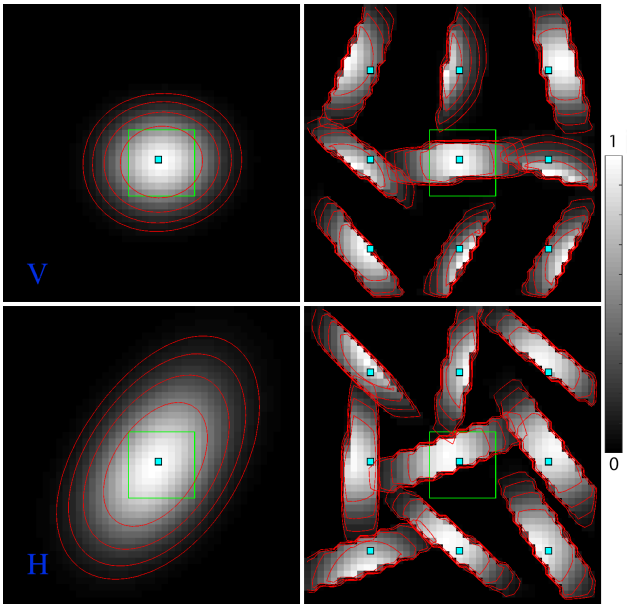

Figure 3: *More detailed illustration of the MRSF of a particular (left column) egg and (right column) slice measurement for (top row) HH-polarization and (bottom row) VV-polarization. The slices shown are from different measurements that happened to cover the same small box (the small filled box). Contours are shown at -3, -6, -9 and -12 dB from the peak response. Image area is 100 km × 100 km. The large square box is 22.25 km. The small box is 2.225 km. For clarity, slices are offset from the center as indicated by the positions of the small squares.*

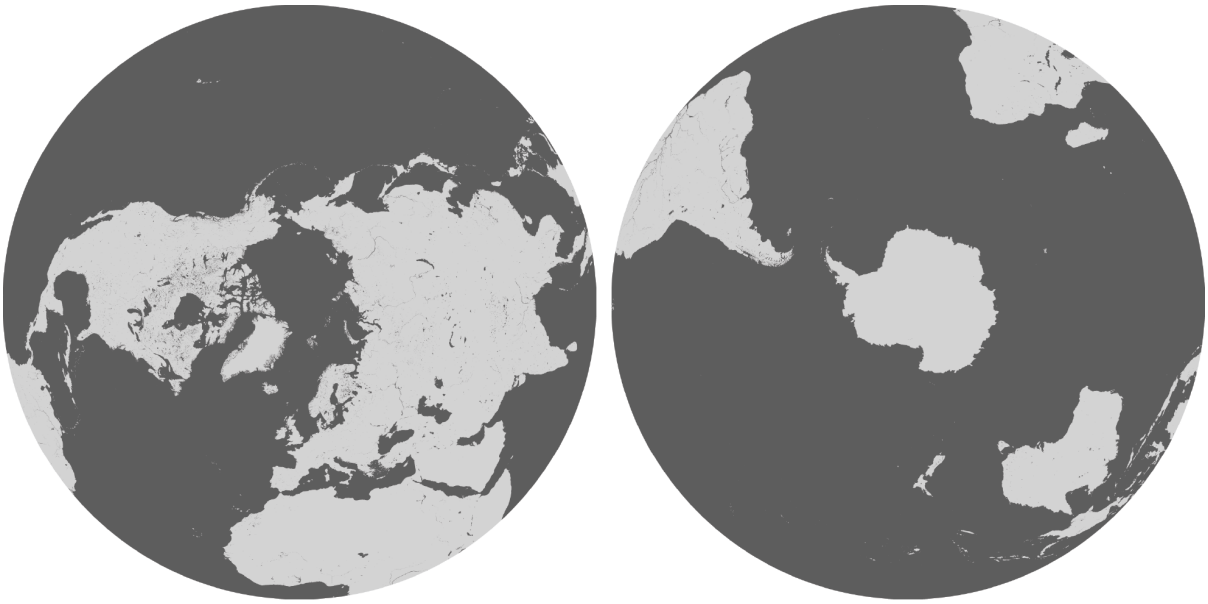

Figure 4: *Northern and Southern EASE-Grid 2.0 projection extents. Land-ocean mask is from Brodzik and Knowles (2011).*

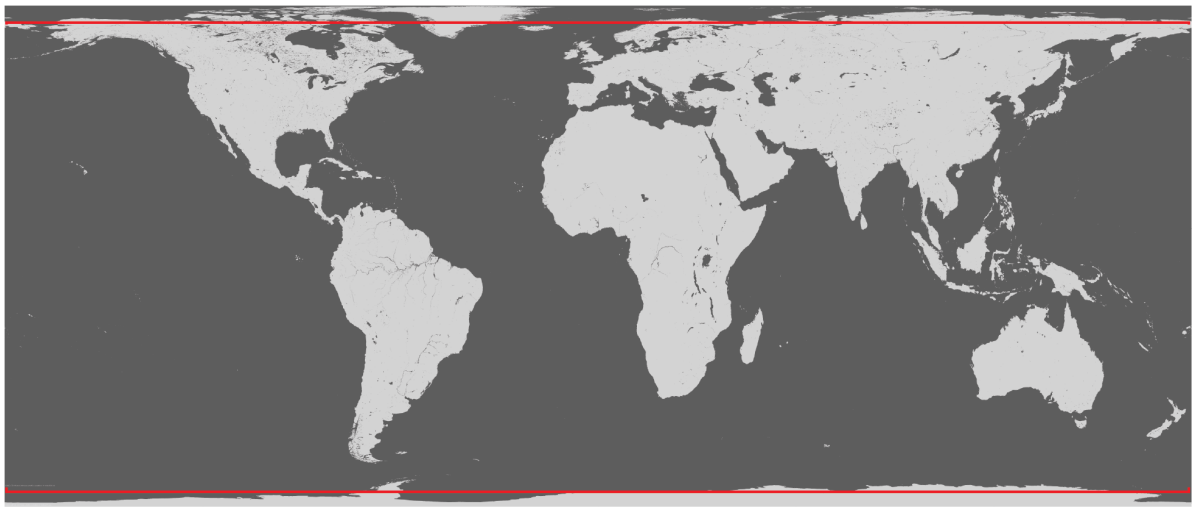

Figure 5: *Cylindrical EASE-Grid 2.0 projection extents. Full extent coverage is EASE2-M, with horizontal red lines delineating the smaller latitudinal extent of the EASE2-T grid. Land-ocean mask is from Brodzik and Knowles (2011).*

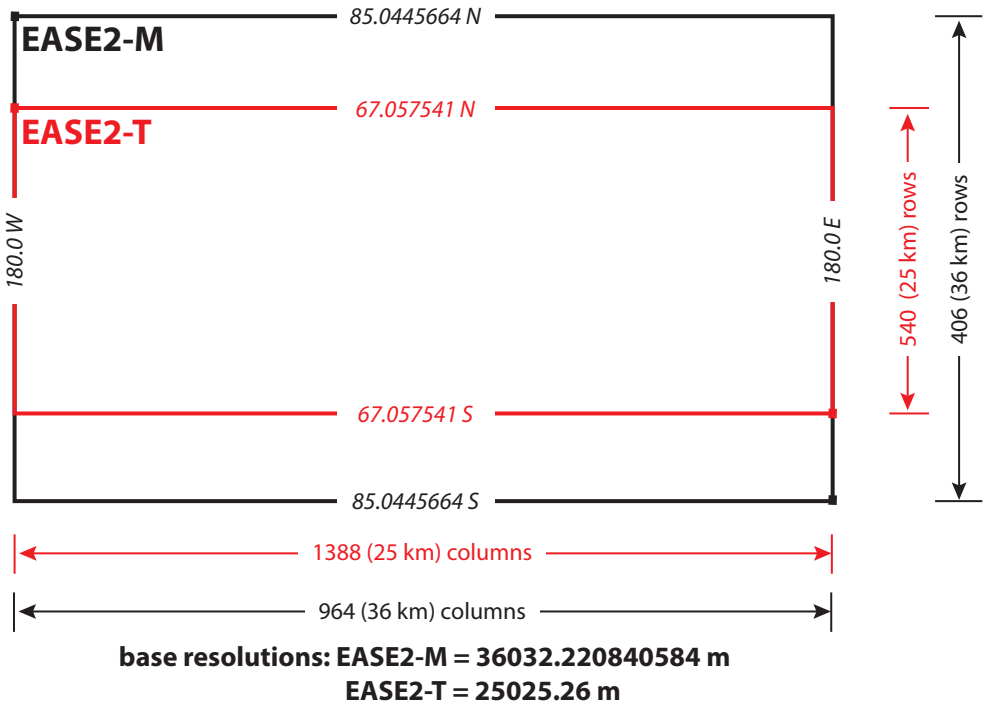

Figure 6: *Relationship between EASE-Grid 2.0 cylindrical projection extents. EASE2-T extent is defined for compatibility with the CETB products. Difference in latitudinal extent is exaggerated, see Fig. 5 for actual difference in projected extent (Brodzik et al., 2021).*

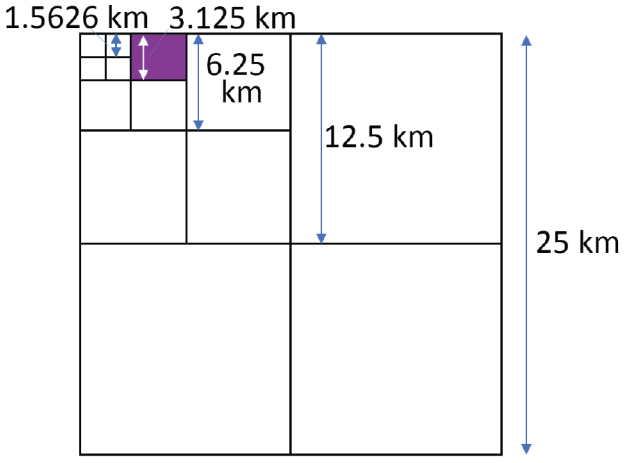

Figure 7: *CETB nested grids based on a 25 km base resolution. Only 25 km and 3.125 km divisions are used in* RapidScat *products (Long et al., 2019).*

5 Algorithm Description

5.1 Background

The *effective resolution* of an image is defined by the *pixel spatial response function* (PSRF), where the effective resolution is given by the dimension(s) of the one-half power (3-dB) extent of the PSRF (Long, 2017a). In contrast, the *measurement spatial response function* (SRF) describes the spatial characteristics of the *individual* measurements. For a radar, the SRF depends on the two-way antenna gain pattern, the scan geometry, and the signal processing. For both radars and radiometers, the PSRF depends on the SRF and the image formation algorithm. In a linear image formation algorithm, the reported pixel value consists of the weighted sum of nearby measurements. In this case the PSRF is then the normalized weighted sum of the measurement SRF functions, including their spatial offset from the center of the pixel. Examples of SeaWinds SRFs and PSRF are available in Long (2017a).

The spacing of pixels is termed the "pixel posting" or the "posting resolution". In creating the *RapidScat* backscatter image product, multiple measurements from different passes are combined into single pixel values. The resulting image pixels have an effective resolution slightly coarser than the posting resolution since (1) the measurements are not all centered the same, and (2) their SRFs can extend outside of the pixel area. The PSRF provides the tool for defining the effective pixel resolution (Long and Brodzik, 2016a). In order to be compatible with the CETB data set, two posting resolutions are considered: 25 km and 3.125 km, see Fig. 8. The former is reserved for GRD products while the finer resolution is used for the resolution-enhanced products.

5.2 *RapidScat* Backscatter Image Products

The *RapidScat* backscatter products include both low-noise (low-resolution) coarse resolution GRD images and higher-noise (enhanced) fine-resolution (SIR) images. The various products have their advantages and disadvantages. Multiple image types allow users the flexibility of choosing the appropriate images for their research application.

To create radar CETB-compatible products, different approaches are used for each resolution. Because the sensor was not designed as an imager, there are gaps between the measurements that must be filled by combining multiple passes over an extended imaging period. As a result of the 4 day near-repeat cycle, two imaging periods are defined: 2 day and 4 day. These provide a user-selectable tradeoff between temporal resolution, spatial resolution, and noise.

For GRD images, the source backscatter measurements are gridded onto a 25 km grid using DIB techniques. In this approach, all the measurements whose center location falls within a grid element are averaged into the reported value. For the 3.125 km product, the

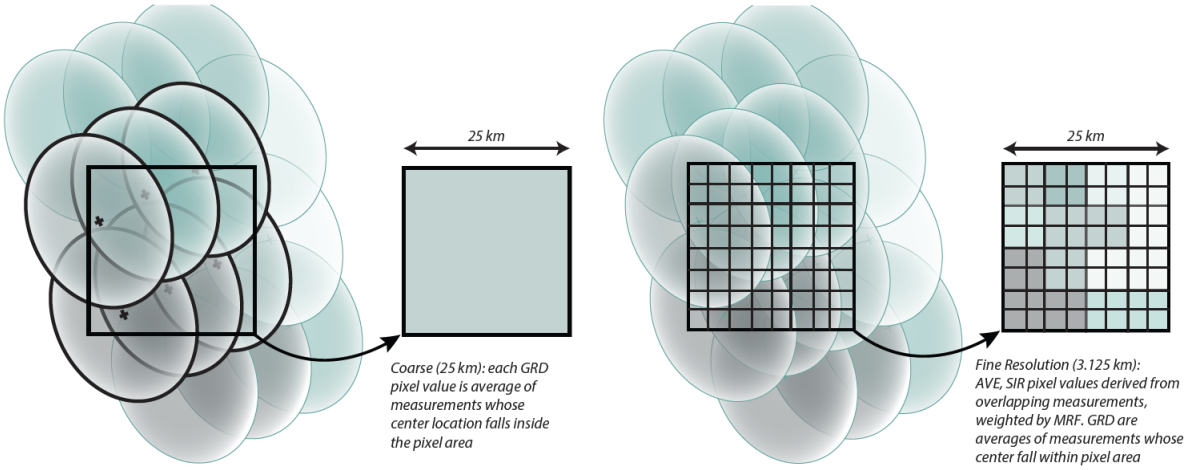

Figure 8: *Conceptual illustration of coarse 25 km (left) vs. high resolution 3.125 km (right) pixels. The ellipses represent the individual SRFs of the egg measurements. DIB is used for GRD images while AVE and SIR are used for high resolution images.*

source measurements are processed using the first iteration of the SIR algorithm (AVE). AVE images use weighted averages where the weighting is the measurement SRF, which may vary from measurement to measurement. Along with each measurement's SRF, the SIR algorithm exploits the irregular patterns of the measurement locations and signal oversampling from overlaps in adjacent footprints and overlapping passes. Table 5 summarizes the image product types.

5.3 Radar Spatial Response and Image Reconstruction

The effective spatial resolution of an image product is determined by the SRF of the sensor and by the image formation algorithm used. As previously noted, the SRF is determined by the antenna gain pattern, the scan geometry (notably the antenna scan angle), and the signal processing, see Long et al. (1993) and Long (2017a). The SRF of SeaWinds measurements are illustrated in Figs. 2 and 3. The goal in forming a σ^o image is to estimate the backscatter properties of the surface from noisy measurements that employ (possibly variable) MSFs that sample the surface. Though simple to implement, DIB techniques ignore the SRF, which limits their effective resolution. Reconstruction techniques that use the SRF can provide much finer effective resolution (Long, 2017a).

Reconstruction processing techniques effectively assume the underlying signal (the backscatter) being sampled is band-limited, which is the only consistent assumption possible with sampled data (Long and Brodzik, 2016b, Long and Franz, 2016b). For reconstruction, the backscatter at each point of a fine-scale pixel grid is estimated, producing a backscatter image or map. While the image is generated on a regular grid, the measurement loca-

tions and MRF are not aligned with the grid, and so the measurements form an irregular sampling pattern, which can complicate signal reconstruction. Many commonly used image formation algorithms either ignore this (as is done in DIB) or attempt to interpolate or distance-weight the measurements values. In using image reconstruction, we avoid these ad hoc, non-optimal approaches and explicitly compute the MRF of each measurement as part of the reconstruction process. This is computationally intense, but provides the best possible image construction. The remainder of this section outlines this process.

An individual scatterometer backscatter measurement z_i can be modeled as the integral of the product of the SRF and the surface backscatter, i.e.,

$$z_i = \iint \text{SRF}_i(x, y; pp)\sigma^o(x, y, \theta, \phi_i, t, pp)dxdy + \text{noise} \tag{2}$$

where $\text{SRF}_i(x, y; pp)$ is the spatial SRF of the ith measurement at x, y, and the surface σ^o depends on spatial location x, y, incidence angle θ, azimuth angle ϕ, time t, and polarization pp, i.e.,

$$\text{SRF}_i(x, y; pp) = \iint \frac{G_a^2(x, y; pp)G_p(x, y; pp)}{R^4(x, y)}. \tag{3}$$

where

$$X = \iint \frac{G_a^2(x, y; pp)G_p(x, y; pp)}{R^4(x, y)}dxdy. \tag{4}$$

where $G_a(x, y; pp)$ is the effective two-way antenna gain at the surface at (x, y) for polarization pp, $G_p(x, y; pp)$ is the processor gain, and $R(x, y)$ is the slant range from the radar to the surface. Note that the measurement is an average of σ^o in spatial coordinates as well as in azimuth and incidence angles.

Eq. 2 is discretized on the imaging grid to become

$$z_i = \sum_{j \in \text{image}} h_{ij}a_j + \text{noise} \tag{5}$$

where a_j is the backscatter at the center of the j^{th} pixel at (x_l, y_k) and $h_{ij} = SRF(x_l, y_k; \phi_i)$ is the discretely sampled SRF for the i-th measurement evaluated at the j-th pixel center where h_{ij} is normalized so that $\sum_j h_{ij} = 1$. In practice, the SRF is negligible some distance from the measurement center, so the sums need only be computed over a small area around the pixel. Ignoring the noise, Eq. 5 can be written as the matrix equation

$$\vec{Z} = \mathbf{H}\vec{a} \tag{6}$$

where $\mathbf{H}$ contains the sampled SRF for each measurement and $\vec{Z}$ and $\vec{a}$ are vectors composed of the measurements z_i and a_j, respectively. Even for small images, $\mathbf{H}$ is large and sparse, and may be over-determined or under-determined depending on the number and

locations of the measurements. Reconstruction of the surface σ^o is equivalent to inverting Eq. 6.

The iterative SIR algorithm (Early and Long, 2001, Long et al., 1993) is a particular reconstruction algorithm that is specifically developed for scatterometer image formation. SIR approximates a maximum-entropy solution to an under-determined equation and a least-squares solution to an over-determined system. The first iteration of SIR is termed 'AVE' (for weighted AVErage) and provides a simple reconstruction estimate that is refined in later SIR iterations. The AVE estimate of the j-th pixel is given by

$$a_j = \frac{\sum_i h_{ij} z_i}{\sum_i h_{ij}} \tag{7}$$

where the sums are over all measurements that have non-negligible SRF at the pixel. The SIR iteration begins with an initial image a_j^0 whose pixels are set to the AVE values defined in Eq. 7. Thereafter, the iterative equation for single-variate SIR is given by

$$a_j^{k+1} = \frac{\sum_i u_{ij}^k h_{ij}}{\sum_i h_{ij}} \tag{8}$$

where

$$u_{ij}^k = \begin{cases} \left[\frac{1}{2p_i^k}\left(1 - \frac{1}{d_i^k}\right) + \frac{1}{a_j^k d_i^k}\right]^{-1} & d_i^k \geq 1 \\ \frac{1}{2}p_i^k(1 - d_i^k) + a_j^k d_i^k & d_i^k < 1 \end{cases} \tag{9}$$

$$d_i^k = \left(\frac{z_i}{p_i^k}\right)^{\lambda} \tag{10}$$

where $d_i^k = (s_i/p_i^k)^\lambda$ with $\lambda = \frac{1}{2}$. The factor d_i^k is the square root of the ratio of a measurement to its forward projection at the k^{th} iteration. The update term u_{ij}^k is a non-linear function of both d_i^k and the previous image a_j^k. The sigmoid-like non-linearity in Eq. 9 constrains the amount of change permitted during any one iteration, thereby minimizing the effects of noise (Long et al., 1993). A spatial median filter can be applied to the image between iterations to further reduce the noise (Long et al., 1993).

For scatterometers, SIR is implemented in dB (Long, 2017a, Early and Long, 2001, Long et al., 1993); i.e., the computation is done on $10\log_{10}(z_i)$ rather than on the linear-space value z_i as done in the radiometer version of SIR (Long and Brodzik, 2016a, Long and Daum, 1998). In considering the differences between linear and dB processing, recall the well-known fact that computing the arithmetic mean of values in dB is equivalent to computing $10\log_{10}$ of the geometric mean of the linear-space values (Wikipedia, 2016). With the measurements in dB, the reconstruction processing can be viewed as a form of weighted geometric mean filtering. Since it has been found that geometric mean filters are better at

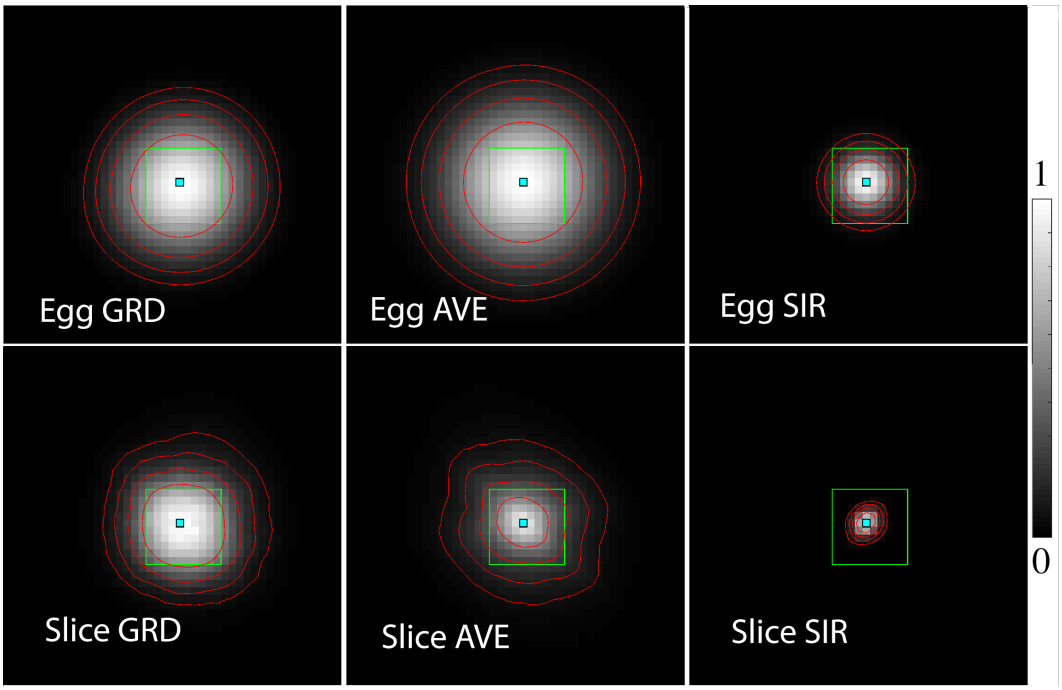

Figure 9: *Comparison of the effective PSRF of pixels for egg and slice image formation. For this illustrative example, the coarse grid is 22.5 km while the fine grid is 2.225 km. This example is for HH-pol, but VV-polarization is similar. The size of each panel is 100 km $\times$ 100 km. Linear gray scale. Contours are shown at -3, -6, -9, and -12 dB from the peak response (Long, 2017a).*

reducing Gaussian-type noise and preserving linear features than (linear) arithmetic mean filters (Pitas and Venetsanopoulos, 1986), some performance advantage to dB processing is expected and observed (Long, 2017a). The linear and dB computations yield similar, but slightly different results, due to the varying signal-to-noise ratio (SNR) of the measurements and limited signal dynamic range (Long, 2017a).

In practice, since the σ^o measurements are quite noisy, attempting full image reconstruction can produce excessive noise enhancement. In general, more iterations improve the signal and resolution, but also increase the noise level. To reduce noise enhancement and resulting artifacts, regularization can be employed, at the expense of resolution (Long and Franz, 2016a, Early and Long, 2001, Long et al., 1993, Long, 2017a). Regularization is a smoothing constraint introduced in an inverse problem to prevent extreme values or over-fitting. Regularization results in partial or incomplete reconstruction of the signal (Long and Franz, 2016a). It also creates a trade off between signal reconstruction accuracy and noise enhancement. SIR includes regularization achieved by prematurely terminating the iteration. Based on simulations and confirmed by analysis of actual data, 20-30 itera-

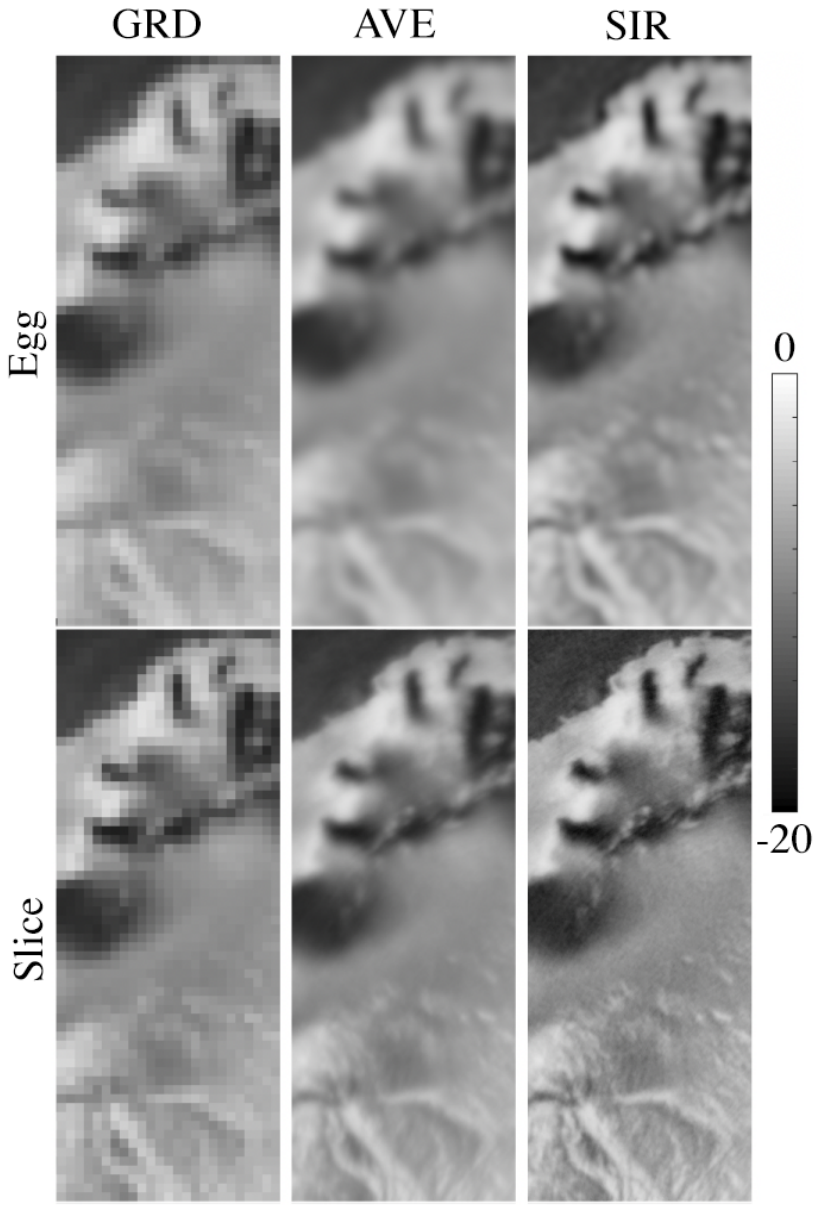

Figure 10: *Extracted QuikSCAT HH-polarization σ^o images created from four days (254-257, 1999) of data for different cases of algorithm. Scale in dB. Note the finer detail apparent in the SIR-enhanced images (Long, 2017a).*

tions provides a nice trade off result Long (2017a). We note that for a noisy sensor like a scatterometer, the results are not particularly sensitive to the precise value chosen, hence a fixed value can be selected. Selection of the number of iterations is based on simulation, see Early and Long (2001), Long et al. (1993) and Long (2017a). For this product, a fixed number (30) of SIR iterations is employed for both eggs and slices.

A comparison of the resulting PSRF of GRD, AVE, and SIR images for eggs and slices is shown in Fig. 9. Note that that SIR PSRF is significantly finer than the non-enhanced GRD and slice PSRFs. Figure 10 compares the resolution of the resulting images for a small area in Antarctica.

5.3.1 Local-Time-of-Day (LTOD)

As previously noted, the goal of image reconstruction is to estimate the surface σ^o from the sensor σ^o measurements. Measurements from multiple orbit passes over a narrow local time window are combined. When multiple measurements are combined, the resulting images represent a temporal average of the measurements over the averaging period. There is an implicit assumption that the surface characteristics remain constant over the imaging period for both conventional-resolution (GRD) and enhanced-resolution (SIR) images.

The radar backscatter of a natural surface is a strong function of the state of the water it contains, i.e., frozen or thawed (Ulaby and Long, 2014). Unlike the sun-synchronous SeaWinds and QuikSCAT platforms, the ISS orbit is NOT sun-synchronous so that over a period of weeks, every location with the coverage area is sampled over the full 24-hour local time of day. For a short period (e.g., a day or two), however, the RapidScat observations at the equator fall within two narrow diurnal windows. (These windows migrate with time.) At the equator, these correspond to the ascending and descending orbit passes. This can be exploited to provide twice-daily sampling. Thus, *RapidScat* images on the cylindrical *EASE-Grid 2.0* projections are separated by ascending and descending passes. A separate image ("both") product is also made. It combines all data over the time period. This maximizes spatial coverage at the expense of temporal resolution. The standard product includes images of the mean LTOD of the observations as well as the standard deviation of the LTOD of the measurements combined into each σ^o image pixel. The mean LTOD image is median-filtered to reduce noise in the estimate. Figs. 11–14 compare and contrast the difference between the both, ascending, and descending σ^o images and the LTOD images.

Figure 11: *Example 1-day RapidScat VV-polarization σ^o images for DOY 283: (top) ascending, (center) descending, (bottom) both passes. Image resolution has been reduced for display.*

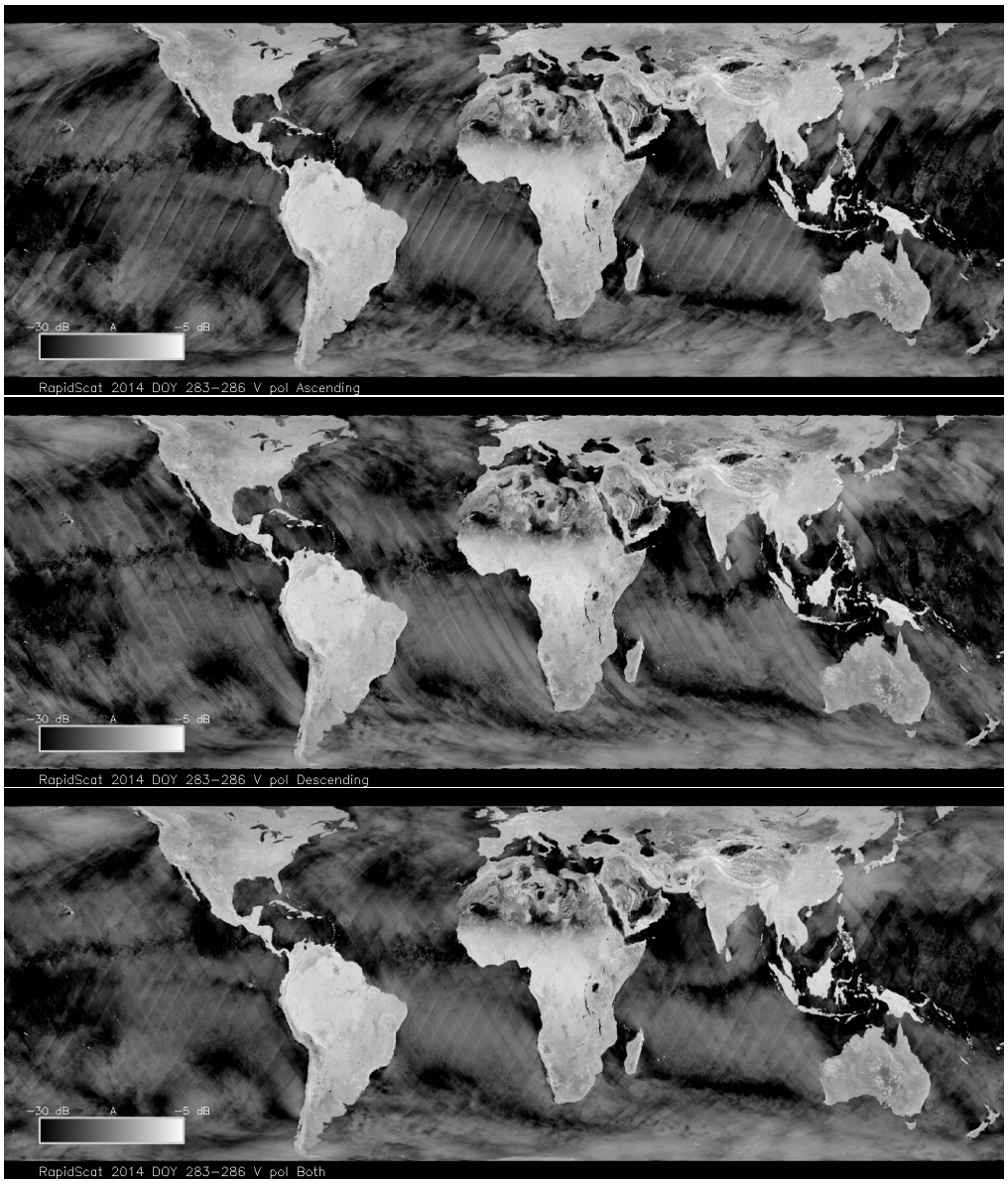

Figure 12: *Example 4-day RapidScat VV-polarization σ^o images for DOY 283-286: (top) ascending, (center) descending, (bottom) both passes. Image resolution has been reduced for display.*

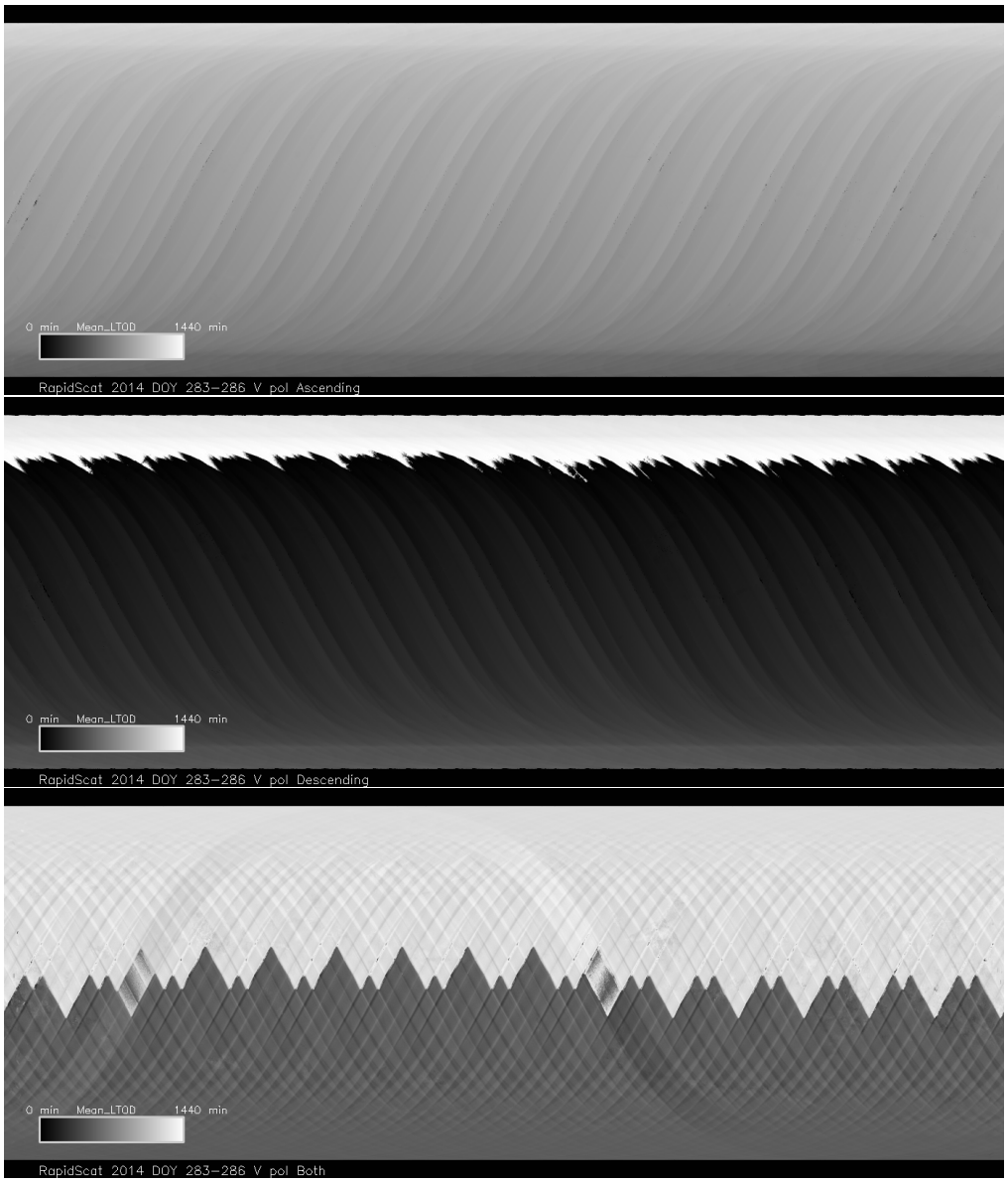

Figure 13: *Example 4-day RapidScat VV-polarization mean local-time-of-day images for DOY 283-286: (top) ascending, (center) descending, (bottom) both passes. Image resolution has been reduced for display. Note that the value is circular, so white and black are adjacent values.*

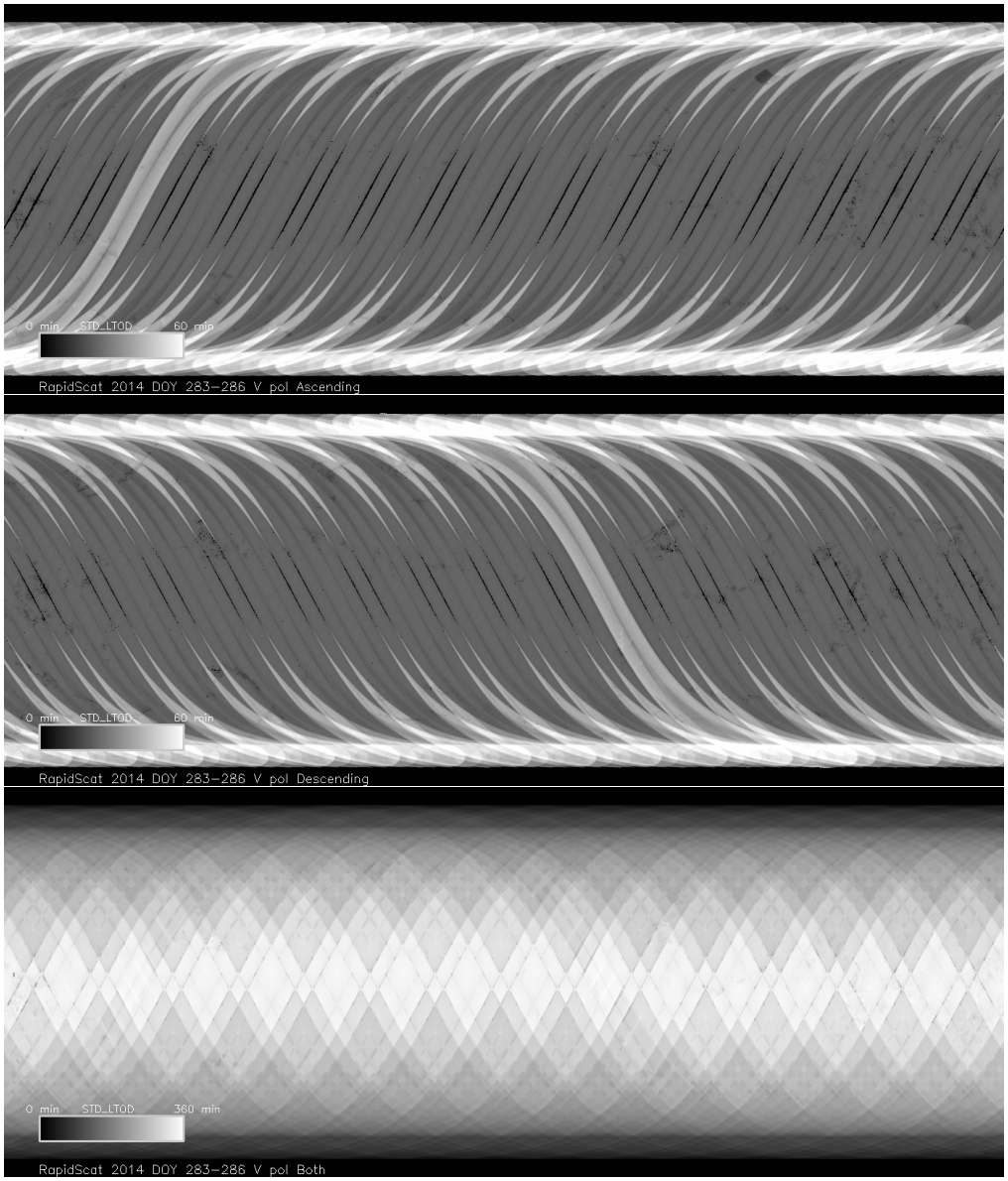

Figure 14: *Example 4-day RapidScat VV-polarization standard deviation of the local-time-of-day images: (top) ascending, (center) descending, (bottom) both passes. Image resolution has been reduced for display. Note the different color scale for the bottom image. Also note that over 4 days, all the ascending passes are within 1 hour of each other and similar for descending passes. The standard deviation of the LTOD is much higher for the bottom image.*

6 Measurement Modeling

6.1 Incidence Angle Effects

Over natural surfaces σ^o depends on the measurement incidence angle (EIA). Since SeaWinds is a pencil-beam system, it collects σ^o measurements at only two incidence angles: nominally 46° for the HH-pol inner beam and 54.1° for the outer VV-pol outer beam. No corrections are made for variations in incidence angle. This differs from fan-beam products which normalize the incidence angle to 40°, e.g., (Long and Miller, 2023a,b, 2024a).

6.2 Azimuth Angle Effects

Periodic natural surfaces exhibit variations in σ^o with azimuth angle, including water waves (Ulaby and Long, 2014, Naderi et al., 1991), sastrugi and snow dunes (Long and Drinkwater, 2000, Lindsley and Long, 2016, Ashcraft and Long, 2006, Long and Miller, 2022). The measured σ^o is thus a function of the azimuth direction from which the surface is observed. Scatterometers such as SeaWinds are *designed* to make multi-azimuth observations over the ocean to exploit this effect for wind-driven waves in order to estimate the near-surface wind (Spencer et al., 2000, Naderi et al., 1991). However, these measurements are intrinsically coarse since they must be made in a single pass. Unlike the ocean, land and ice features do not (generally) change as rapidly so observations from multiple passes can be combined.

Over the course of the orbit's repeat cycle each point on the surface can be observed at multiple azimuth angles (Spencer et al., 2000). For example, as the spacecraft passes over a particular location within the swath, the location is first observed looking forward, then a short while later the same location is observed looking backward. Over the orbit repeat cycle, the ground track shifts so that the same location is observed from a different set of azimuth angles for each pass. The precise distribution of azimuth angles depends on the orbit latitude, with the narrowest range near the equator and the largest range at high latitudes.

Note that there is a trade off between the imaging time period, the spatial resolution, and the azimuth sampling (Long, 2017b). Short time periods provide better temporal resolution for tracking sea ice motion and rapid freeze thaw events. However, short time periods provide inadequate coverage and/or azimuth sampling to reliably estimate the azimuth angle variation, particularly when the data is divided by local time of day. Recalling that the orbit repeat cycle is near-repeat after 4 days, we choose N_d =4 imaging intervals (N_d in days)[4]. The imaging intervals are chosen to overlap by $N_d - 1$ days so they act like a N_d long moving average filter. Shorter N_d provides finer temporal resolution at the expense of reduced spatial coverage/resolution, including possible spatial artifacts in the reconstruction.

[4]Imaging intervals are specified in days, but may include only morning or evening (or descending or ascending) passes depending on the LTOD setting.

These negative effects are reduced for the longer imaging intervals.

Note that a particular σ^o observation is an average of σ^o in spatial coordinates as well as in azimuth and incidence angles. Within a single measurement the azimuth angle span ($<1^\circ$) for a particular measurement is small and can be neglected. The incidence angle span within a single measurement can be slightly larger ($\sim$1-1.5°). The roll off of σ^o vs. incidence angle slightly biases the integrated measurement toward smaller incidence angles. However, this effect is neglected in the *RapidScat* product.

On the other hand, the variation in σ^o as a function of azimuth and incidence angles for different measurements is important and provides useful geophysical information, particularly in the polar regions. Incidence angle variation is considered in the previous section. Of source, the variation in σ^o as a function of azimuth enables wind retrieval over the ocean citepnaderi,ulaby2014,meissner2017. Azimuth variation (sometimes termed 'azimuth modulation') can be observed over snow dunes and sastrugi (Long and Drinkwater, 2000, Ashcraft and Long, 2006, Lindsley and Long, 2016) and sand dunes in ergs[5] (Stephen and Long, 2007). As a result, significant azimuth variation in σ^o is common over the Great Ice Sheets (GI) of Greenland and Antarctica, but is only rarely observed elsewhere over large regions with the exceptions of ergs.

Since each satellite pass observes a given point on the surface from a limited azimuth angle, the variation of σ^o with azimuth can lead to biases in the mean σ^o value and to imaging artifacts when multiple passes with different azimuth angle observations are combined. To deal with azimuth variation of σ^o on the GI, previous investigators, e.g., Long and Drinkwater (2000) Ashcraft and Long (2006), and Lindsley and Long (2016), have used a simple Fourier series model for the azimuth variation observed in σ^o. Two models have been considered (Long and Miller, 2022, 2023a). Here, the fixed azimuth (FA) modulation coefficient model is used at a fixed incidence angle as determined by the beam polarization. The azimuth modulation model employed can be expressed as

$$\sigma^0 = A + M_1 \cos(\phi + P_1) + M_2 \cos(2\phi + P_2) \tag{11}$$

where ϕ is the azimuth angle, $M_1 = A_1$ and $M_2 = A_2$ for the FA model and P_1 and P_2 are the phase angles relative to north. Note that the model can be with σ^o in dB or linear space, though dB models have proven to the the most successful (Long and Drinkwater, 2000, Lindsley and Long, 2016). Other azimuth modulation studies can be found in Ashcraft and Long (2006), Long and Drinkwater (2000), and Long and Miller (2022, 2023a, 2024b).

We note that most Ku-band azimuth modulation is observed in the polar regions, which are not covered by RapidScat. Thus, to minimize the size of the *RapidScat* product, azimuth modulation products are NOT included in the E2T regions in the product.

The PSRF is defined by the weighted combination of the MRFs of the measurements included in the pixel value. The weighting is determined by the choice of the algorithm

[5]An erg landform is a large region or 'sea' of vegetation-free, wind-swept desert sand.

used to create the image (Long, 2017a). This summation can be done in linear space (i.e., not in dB) or in dB. As noted in Section 5.3, the latter is used for SIR. When multiple overlapping measurements are available, i.e., the surface is oversampled, it is possible to obtain images with finer effective resolution.

Enhancement of the effective resolution *requires* dense sampling of the surface. This is the reason multiple passes are used. In addition, multiple measurements at a diversity of incidence angles are required to estimate the incidence angle slope. When the surface is adequately sampled, the effective spatial resolution is improved, which can result in a reduction in noise. However, when the surface is undersampled, it is difficult for the image resolution to be much better than the SRF resolution.

6.3 Data Volume

Table 5 summarizes available CETB *RapidScat* radar products, which are all in CETB-standard EASE-2 Grid projections and netcdf4 file format. In this table, "days" refers to the length of time used for image formation. Imaging periods overlap, with a new image started each day. Note that for LTOD images that in order to have the right number of morning or evening passes, the time period of the measurements actually used in the images may extend slightly outside the multi-day period. Individual file sizes vary due to internal file compression for each image type. See Section 4.6 for access details.

7 Acknowledgements

This work utilizes resources from the Brigham Young University Scatterometer Climate Record Pathfinder and University of Colorado Boulder Research Computing Group, which is supported by the National Science Foundation (awards TBD), the University of Colorado Boulder and Colorado State University.

8 References

References

Ashcraft, I. S. and D. G. Long. 2006. Relating microwave backscatter azimuth modulation to surface properties of the Greenland ice sheet. *Journal of Glaciology 52*(177), 257–266. doi:10.3189/172756506781828764.

Brodzik, M., D. Long, M. Hardman, A. Paget, and R. Armstrong. 2016. MEaSUREs calibrated enhanced-resolution passive microwave daily EASE-grid 2.0 brightness temperature ESDRAlgorithm Theoretical Basis Document, version 2. doi:https://doi.org/10.5067/MEASURES/CRYOSPHERE/NSIDC-0630.002.

Brodzik, M. J., B. Billingsley, T. Haran, B. Raup, and M. H. Savoie. 2012. EASE-Grid 2.0: Incremental but significant improvements for Earth-gridded data sets. *International Society for Photogrammetry and Remote Sensing 1*, 32–45. doi:10.3390/ijgi101003.

Brodzik, M. J., B. Billingsley, T. Haran, B. Raup, and M. H. Savoie. 2014. Correction: Brodzik, M.J., *et al.* EASE-Grid 2.0: Incremental but Significant Improvements for Earth-Gridded Data Sets, *ISPRS Int. J. Geo-Inf.* 2012, 1, 32–45. *ISPRS Int. J. Geo-Inf. 3*, 1154–1156. doi:10.3390/ijgi3031154.

Brodzik, M. J. and K. Knowles. 2011. EASE-Grid 2.0 Land-Ocean-Coastline-Ice Masks Derived from Boston University MODIS/Terra Land Cover Data. NASA National Snow and Ice Data Center DAAC, Boulder, CO USA. Digital Media, http://nsidc.org/data/nsidc-0610, doi:https://doi.org/10.5067/XR8523MC24TB.

Brodzik, M. J., D. G. Long, M. A. Hardman, A. Paget, and R. L. Armstrong. 2016, updated 2021. MEaSUREs Calibrated Enhanced-Resolution Passive Microwave Daily EASE-Grid 2.0 Brightness Temperature ESDR, Version 1. National Snow and Ice Data Center, Boulder, CO USA. Digital Media, http://nsidc.org/data/nsidc-0630, doi:https://doi.org/10.5067/MEASURES/CRYOSPHERE/NSIDC-0630.001.

Brodzik, M. J., J. M. Ramage, M. A. Hardman, D. G. Long, and R. L. Armstrong. 2018. Improving melt onset detection in mountainous regions from the new, enhanced-resolution passive microwave climate record. Poster presentation at EGU General Assembly, CR 2.1:10690, Vienna, Austria, 9–13 April.

Durden, S. L. and D. Perkovic-Martin. 2017. The rapidscat ocean winds scatterometer: A radar system engineering perspective. *IEEE Geoscience and Remote Sensing Magazine 5*(3), 36–43. doi:10.1109/MGRS.2017.2678999.

Early, D. S. and D. G. Long. 2001. Image reconstruction and enhanced resolution imaging from irregular samples. *IEEE Transactions on Geoscience and Remote Sensing 39*(2), 291–302. doi:10.1109/36.905237.

Fore, A., B. Stiles, A. Chau, B. Williams, R. S. Dunbar, and R. E.. 2013. Point-wise wind retrieval and ambiguity removal improvements for the QuikSCAT climatological data set. *IEEE Trans. Geoscience and Remote Sensing 52*(1), 51–59. doi:10.1109/TGRS.2012.2235843.

Lindsley, R. and D. Long. 2016. ASCAT and QuikSCAT azimuth modulation of backscatter over East Antarctica. *IEEE Geoscience and Remote Sensing Letters, 13*(8), 1134–1138. doi:10.1109/LGRS.2016.2572101.

Long, D. and M. Brodzik. 2016a. Optimum image formation for spaceborne microwave radiometer products. *IEEE Trans. Geosci. Remote Sensing 54*(5), 2763–2779. doi:10.1109/TGARS.2015.2505677.

Long, D. and D. Daum. 1998. Spatial resolution enhancement of SSM/I data. *IEEE Trans. Geosci. Remote Sensing 36*(2), 407–417. doi:10.1109/36.662726.

Long, D. and M. Drinkwater. 2000. Azimuth variation in microwave scatterometer and radiometer data over Antarctica. *IEEE Transactions on Geoscience and Remote Sensing 38*(4), 1857–1870. doi:10.1109/36.851769.

Long, D. and R. Franz. 2016a. Band-limited signal reconstruction from irregular samples with variable apertures. *IEEE Transactions on Geoscience and Remote Sensing 54*(4), 2424–2436. doi:10.1109/TGRS.2015.2501366.

Long, D., P. Hardin, and P. Whiting. 1993. Resolution enhancement of spaceborne scatterometer data. *IEEE Trans. Geosci. Remote Sensing 31*(3), 700–715. doi:10.1109/36.225536.

Long, D. and J. Z. Miller. 2022. SMAP radar SAR and SIR-enhanced twice-daily EASE-grid 2.0 radar backscatter Algorithm Theoretical Basis Document. doi:https://doi.org/10.5067/SCKWZSWQ7HPL.

Long, D. and J. Z. Miller. 2023a. NSCAT twice-daily SIR-enhanced scatterometer EASE-grid 2.0 radar backscatter Algorithm Theoretical Basis Document. doi:https://doi.org/10.5281/zenodo.11199226.

Long, D. and J. Z. Miller. 2023b. SASS twice-daily SIR-enhanced scatterometer EASE-grid 2.0 radar backscatter Algorithm Theoretical Basis Document. doi:https://doi.org/10.5281/zenodo.11187073.

Long, D. and J. Z. Miller. 2024a. ASCAT twice-daily SIR-enhanced scatterometer EASE-grid 2.0 radar backscatter Algorithm Theoretical Basis Document. doi:https://doi.org/10.5281/zenodo.14582508.

Long, D. and J. Z. Miller. 2024b. QuikSCAT/SeaWinds twice-daily SIR-enhanced scatterometer EASE-grid 2.0 radar backscatter Algorithm Theoretical Basis Document. doi:https://doi.org/10.5281/zenodo.14582418.

Long, D. G.. 2017a. Comparison of SeaWinds backscatter imaging algorithms. *IEEE J. Sel. Topics in Applied Earth Observations 10*(3), 2214–2231. doi:10.1109/JSTARS.2016.2626966.

Long, D. G.. 2017b. Comparison of SeaWinds Backscatter Imaging Algorithms. *IEEE Journal of Selected Topics in Applied Earth Observations 10*(3), 2214–2231. doi:10.1109/JSTARS.2016.2626966.

Long, D. G.. 2017c. Polar applications of spaceborne scatterometers. *IEEE Journal of Selected Topics in Applied Earth Observations 10*(3), 2307–2320. doi:10.1109/JSTARS.2016.2629418.

Long, D. G. and M. J. Brodzik. 2016b, May. Optimum Image Formation for Spaceborne Microwave Radiometer Products. *IEEE Transactions on Geoscience and Remote Sensing 54*(5), 2763–2779. doi:10.1109/TGRS.2015.2505677.

Long, D. G., M. J. Brodzik, and M. A. Hardman. 2019. Enhanced–Resolution SMAP Brightness Temperature Image Products. *IEEE Transactions on Geoscience and Remote Sensing 57*(7), 4151–4163. doi:10.1109/TGRS.2018.2889427.

Long, D. G. and R. O. W. Franz. 2016b. Band–limited Signal Reconstruction from Irregular Samples with Variable Apertures. *IEEE Transactions on Geoscience and Remote Sensing 54*(4), 2424–2436. doi:10.1109/TGRS.2015.2501366.

Madsen, N. M. and D. G. Long. 2016. Calibration and validation of the rapidscat scatterometer using tropical rainforests. *IEEE Transactions on Geoscience and Remote Sensing 54*(5), 2846–2854. doi:10.1109/TGRS.2015.2506463.

Naderi, F., M. H. Freilich, and D. G. Long. 1991. Spaceborne radar measurement of wind velocity over the ocean–an overview of the NSCAT scatterometer system. *Proceedings of the IEEE 79*(6), 850–866. doi:10.1109/5.90163.

Paget, A. P., D. G. Long, and N. M. Madsen. 2016. Rapidscat diurnal cycles over land. *IEEE Transactions on Geoscience and Remote Sensing 54*(6), 3336–3344. doi:10.1109/TGRS.2016.2515022.

Perry, K.. 2001. QuikSCAT Science Data Products User's Manual, ver. 2.1. Document D-18053, Jet Propulsion Laboratory, Pasadena, CA, 2001.

Pitas, I. and A. Venetsanopoulos. 1986. Nonlinear mean filters in image processing. *IEEE Transactions on Acoustics, Speech, and Signal Processing 34*(3), 573–584. doi:10.1109/TASSP.1986.1164857.

Project, R.. 2025. RapidScat Level 1B time-ordered geo-located sigma-0 version 2.0. doi:https://doi.org/10.5067/RSCAT-L1B20.

Spencer, M. W., W.-Y. Tsai, and D. G. Long. 2003. High resolution measurements with a spaceborne pencil-beam scatterometer using combined range/doppler discrimination techniques. *IEEE Transactions on Geoscience and Remote Sensing 41*(3), 567–481. doi:10.1109/TGRS.2003.809938.

Spencer, M. W., C. Wu, and D. G. Long. 2000. Improved resolution backscatter measurements with the seawinds pencil-beam scatterometer. *IEEE Transactions on Geoscience and Remote Sensing 38*(1), 89–104. doi:10.1109/36.823904.

Stephen, H. and D. G. Long. 2007. Spatial and temporal behavior of microwave backscatter directional modulation over the Saharan ergs. *IEEE Transactions on Geoscience and Remote Sensing 45*(5), 1164–1173. doi:10.1109/TGRS.2007.892584.

Ulaby, F. T. and D. G. Long. 2014. *Microwave Radar and Radiometric Remote Sensing*. Ann Arbor, MI, USA: University of Michigan Press.

Wikipedia. visited 8 Oct. 2016. Geometric mean. Online, http://en.wikipedia.org/wiki/Geometric_mean.

Appendices

A *RapidScat* Projections and Grids

Table 6: RapidScat *25 km product EASE-Grid 2.0 projections and grid dimensions, produced for compatibility with CETB ESDR data products (Brodzik et al., 2021).*

Name	Projection	Resolution (km)	Cols	Rows	Latitude Extent	Longitude Extent
EASE2-T25km	Temperate and Tropical Cylindrical	25.02526000	1388	540	±67.0576406°	±180°
EASE2-T3.125km	Temperate and Tropical Cylindrical	3.12815750	11104	4320	±67.0576406°	±180°

Note: While the CETB product definitions include polar regions, these are not produced for RapidScat products since RapidScat does not provide coverage in these regions.

B *RapidScat* Data Definition

B.1 File Requirements

Following Brodzik et al. (2021), *RapidScat* product file requirements as implemented for the *RapidScat* product include:

- File size maximum is less < 4 MB
- Files conform to netCDF-CF 1.6 conventions for all but the requirement that puts the lat/lon arrays into the file; however, CF-compliant coordinate variables with projected coordinate locations are included
- Files pass CF-compliance-checking for all but the lat/lon arrays using the JPL compliance-checker
- Each file contains 1 or more array variables, with associated ancillary variables, possibly different ancillary variables for each gridding technique
- Each file of the same type (GRD or SIR) contains the same file-level metadata for that type
- Time values are machine- and human-readable
- Projection metadata may be in multiple forms (a proj4 string and/or a WKT string)
- Variable/attribute names CF-compliant whenever possible

The *RapidScat* .nc files work with gdal utility, *gdal_translate*, to produce a geoTIFF version of each of the data variables <variable_name> in the file, (details in Brodzik et al. (2018)), for e.g.:

```
$ gdal_translate -of GTiff -b 1 \
NETCDF:''cetb.nc'':<variable_name> variable_name.tif
```

B.2 Filename Convention

RapidScat data are distributed by the NSIDC DAAC (http://nsidc.org/data/nsidc-TBD). Filenames are:
<product-id>_<platform-sensor>_<type>_<algorithm>_<grid-name>_<pass>_<channel>_<yyyymmdd>-<yyyymmdd>_<version>.nc
where parts of the filename are described in Table 7.

Table 7: RapidScat *File Naming Convention*

Part	Description	Values
<product_id>	NSIDC unique data product id	NSIDC-0809
<platform>	Satellite platform	ISS
<sensor>	Sensor name	RapidScat
<type>	Measurement type	one of: • Foot • Slice
<algorithm>	Reconstruction algorithm	one of: • GRD • SIR
<grid_name>	EASE-Grid 2.0 grid id	one of: • EASE2_T25km • EASE2_T3.125 See Table 6
<pass>	Pass direction (T grids)	one of: • B = Both (all measurements) • A = Ascending • D = Descending
<channel_id>	Channel (frequency in GHz and polarization)	13.4 followed by polarization, one of: • HH = horizontal-horizontal • VV = vertical-vertical
<yyyymmdd>	Start date	4-digit year, 2-digit month, and 2-digit day-of-year
<yyyymmdd>	Stop date	4-digit year, 2-digit month, and 2-digit day-of-year
<version>	Version number	production version number

B.3 File Content, v1.0

The following is a sample NetCDF *ncdump –h* utility output for a 4 day *RapidScat* v1.0 3.125 km SIR file. File-level metadata and processing details vary depending on projection, spatial resolution and processing details (method, input file list, etc.).

```
netcdf NSIDC-0809_ISS_RapidScat_Foot_SIR_EASE2_T3.125KM_B_13.4VV_20160701-20160704_V1.0
dimensions:
 time = UNLIMITED ; // (1 currently)
 y = 4320 ;
 x = 11104 ;
variables:
 double time(time) ;
  time:standard_name = "time" ;
  time:coverage_content_type = "coordinate" ;
  time:long_name = "ANSI date" ;
  time:units = "days since 1972-01-01 00:00:00" ;
  time:calendar = "gregorian" ;
  time:axis = "T" ;
  time:valid_range = 0., 1.79769313486232e+308 ;
 double y(y) ;
  y:standard_name = "projection_y_coordinate" ;
  y:coverage_content_type = "coordinate" ;
  y:long_name = "y" ;
  y:units = "meters" ;
  y:axis = "Y" ;
  y:valid_range = -6756820.2, 6756820.2 ;
 double x(x) ;
  x:standard_name = "projection_x_coordinate" ;
  x:coverage_content_type = "coordinate" ;
  x:long_name = "x" ;
  x:units = "meters" ;
  x:axis = "X" ;
  x:valid_range = -17367530.44, 17367530.44 ;
 char crs ;
  crs:grid_mapping_name = "lambert_cylindrical_equal_area" ;
  crs:longitude_of_central_meridian = 0. ;
  crs:standard_parallel = 30. ;
  crs:false_easting = 0. ;
  crs:false_northing = 0. ;
  crs:semi_major_axis = 6378137. ;
```

```
  crs:inverse_flattening = 298.257223563 ;
  crs:proj4text = "+proj=cea +lat_0=0 +lon_0=0 +lat_ts=30 +x_0=0 +y_0=0 +ellps=WGS84 +da
  crs:srid = "urn:ogc:def:crs:EPSG::6933" ;
  crs:coverage_content_type = "auxiliaryInformation" ;
  crs:references = "[\"EASE-Grid 2.0 documentation: http://nsidc.org/data/ease/ease_grid
  crs:crs_wkt = "PROJCRS[\"WGS 84 / NSIDC EASE-Grid 2.0 Global\", BASEGEODCRS[\"WGS 84\"
  crs:long_name = "EASE2_T3.125km" ;
 short Sigma0_ave(time, y, x) ;
  Sigma0_ave:long_name = "AVE Sigma0" ;
  Sigma0_ave:units = "1" ;
  Sigma0_ave:comment_on_units = "unitless, stored as dB=10*log10()" ;
  Sigma0_ave:_FillValue = -32768s ;
  Sigma0_ave:valid_range = 0s, 32767s ;
  Sigma0_ave:packing_convention = "netCDF" ;
  Sigma0_ave:packing_convention_description = "unpacked = scale_factor*packed + add_offs
  Sigma0_ave:scale_factor = 0.002f ;
  Sigma0_ave:add_offset = -55.f ;
  Sigma0_ave:grid_mapping = "crs" ;
  Sigma0_ave:coverage_content_type = "image" ;
 short Sigma0(time, y, x) ;
  Sigma0:long_name = "SIR Sigma0" ;
  Sigma0:units = "1" ;
  Sigma0:comment_on_units = "unitless, stored as dB=10*log10()" ;
  Sigma0:_FillValue = -32768s ;
  Sigma0:valid_range = 0s, 32767s ;
  Sigma0:packing_convention = "netCDF" ;
  Sigma0:packing_convention_description = "unpacked = scale_factor*packed + add_offset"
  Sigma0:scale_factor = 0.002f ;
  Sigma0:add_offset = -55.f ;
  Sigma0:grid_mapping = "crs" ;
  Sigma0:coverage_content_type = "image" ;
  Sigma0:sir_number_of_iterations = 30 ;
  Sigma0:median_filter = 0 ;
  Sigma0:temporal_division = "Both" ;
  Sigma0:frequency_and_polarization = "13.4VV" ;
 short Sigma0_num_samples(time, y, x) ;
  Sigma0_num_samples:long_name = "SIR Number of Measurements" ;
  Sigma0_num_samples:units = "count" ;
  Sigma0_num_samples:_FillValue = 0s ;
  Sigma0_num_samples:valid_range = 1s, 255s ;
```

```
 Sigma0_num_samples:grid_mapping = "crs" ;
 Sigma0_num_samples:coverage_content_type = "auxiliaryInformation" ;
short Incidence_angle(time, y, x) ;
 Incidence_angle:standard_name = "angle_of_incidence" ;
 Incidence_angle:long_name = "SIR Incidence Angle" ;
 Incidence_angle:units = "degree" ;
 Incidence_angle:_FillValue = -1s ;
 Incidence_angle:valid_range = 0s, 9000s ;
 Incidence_angle:packing_convention = "netCDF" ;
 Incidence_angle:packing_convention_description = "unpacked = scale_factor*packed + add
 Incidence_angle:scale_factor = 0.01f ;
 Incidence_angle:add_offset = 0.f ;
 Incidence_angle:grid_mapping = "crs" ;
 Incidence_angle:coverage_content_type = "auxiliaryInformation" ;
short Sigma0_std_dev(time, y, x) ;
 Sigma0_std_dev:long_name = "SIR Sigma0 standard deviation" ;
 Sigma0_std_dev:units = "1" ;
 Sigma0_std_dev:comment_on_units = "unitless, stored as dB=10*log10()" ;
 Sigma0_std_dev:_FillValue = -32768s ;
 Sigma0_std_dev:valid_range = -32766s, 32767s ;
 Sigma0_std_dev:packing_convention = "netCDF" ;
 Sigma0_std_dev:packing_convention_description = "unpacked = scale_factor*packed + add_
 Sigma0_std_dev:scale_factor = 0.002f ;
 Sigma0_std_dev:add_offset = 0.f ;
 Sigma0_std_dev:grid_mapping = "crs" ;
 Sigma0_std_dev:coverage_content_type = "auxiliaryInformation" ;
short Sigma0_time(time, y, x) ;
 Sigma0_time:long_name = "Time of Day" ;
 Sigma0_time:units = "minutes since 2016-07-01 00:00:00" ;
 Sigma0_time:_FillValue = -32768s ;
 Sigma0_time:valid_range = -32767s, 32767s ;
 Sigma0_time:packing_convention = "netCDF" ;
 Sigma0_time:packing_convention_description = "unpacked = scale_factor*packed + add_off
 Sigma0_time:scale_factor = 1.f ;
 Sigma0_time:add_offset = 0.f ;
 Sigma0_time:grid_mapping = "crs" ;
 Sigma0_time:coverage_content_type = "auxiliaryInformation" ;
 Sigma0_time:calendar = "gregorian" ;
short Mean_LTOD(time, y, x) ;
 Mean_LTOD:long_name = "GRD Mean Local Time of Day" ;
```

```
  Mean_LTOD:units = "minutes" ;
  Mean_LTOD:comments = "LTOD=UTCminutes_in_day+4*longitude_in_deg" ;
  Mean_LTOD:_FillValue = -32768s ;
  Mean_LTOD:valid_range = 0s, 1440s ;
  Mean_LTOD:packing_convention = "netCDF" ;
  Mean_LTOD:packing_convention_description = "unpacked = scale_factor*packed + add_offse
  Mean_LTOD:scale_factor = 0.1f ;
  Mean_LTOD:add_offset = 0.f ;
  Mean_LTOD:grid_mapping = "crs" ;
  Mean_LTOD:coverage_content_type = "auxiliaryInformation" ;
 short STD_LTOD(time, y, x) ;
  STD_LTOD:long_name = "GRD STD of Local Time of Day" ;
  STD_LTOD:units = "minutes" ;
  STD_LTOD:comments = "LTOD=UTCminutes_in_day+4*longitude_in_deg" ;
  STD_LTOD:_FillValue = -32768s ;
  STD_LTOD:valid_range = 0s, 1440s ;
  STD_LTOD:packing_convention = "netCDF" ;
  STD_LTOD:packing_convention_description = "unpacked = scale_factor*packed + add_offset
  STD_LTOD:scale_factor = 0.05f ;
  STD_LTOD:add_offset = 0.f ;
  STD_LTOD:grid_mapping = "crs" ;
  STD_LTOD:coverage_content_type = "auxiliaryInformation" ;

// global attributes:
  :references = "Early, D. S., and D.G. Long. 2001. Image Reconstruction and Enhanced Re
  :title = "RapidScat Twice-Daily SIR-Enhanced Scatterometer EASE-Grid 2.0 Radar Backsca
  :id = "doi:10.5067/MTQUFEXMZ3EE" ;
  :summary = "Enhanced-resolution, gridded SeaWinds Ku-band radar backscatter\n" ;
  :project = "Scatterometer Climate Record Pathfinder" ;
  :contributor_name = "David G. Long, NASA Scatterometer Climate Record Pathfinder" ;
  :contributor_role = "Principal Investigator and Developer, Data Producer" ;
  :citation = "Long, D.G., and J.Z. Miller, 2026. RapidScat Twice-Daily SIR-Enhanced Sca
  :license = "These data are freely, openly, and fully available to use without\nrestric
  :Conventions = "CF-1.6, ACDD-1.3" ;
  :product_version = "v1.0" ;
  :software_version_id = "BYU03.00" ;
  :software_repository = "" ;
  :history = "ruev-E2T16-183-186.setup" ;
  :comment = "Epoch date for data in this file: 2016-07-01 00:00:00Z" ;
  :source = ": See input_fileN list and number_of_input_files attributes" ;
```

```
:metadata_link = "http://www.scp.byu.edu/" ;
:institution = "Scatterometer Climate Record Pathfinder\nElectrical and Computer Engin
:publisher_name = "Scatterometer Climate Record Pathfinder" ;
:publisher_type = "institution" ;
:publisher_url = "http://www.scp.byu.edu" ;
:publisher_email = "long@ee.byu.edu" ;
:program = "NASA Earth Science Data and Information System (ESDIS)" ;
:standard_name_vocabulary = "CF Standard Name Table (v27, 28 September 2013)" ;
:cdm_data_type = "Grid" ;
:keywords = "EARTH SCIENCE > SPECTRAL/ENGINEERING > MICROWAVE > RADAR BACKSCATTER" ;
:keywords_vocabulary = "NASA Global Change Master Directory (GCMD) Earth Science Keywo
:platform = "RapidScat > RapidScat Scatterometer on ISS" ;
:platform_vocabulary = "RapidScat > RapidScat Scatterometer on ISS" ;
:instrument = "RapidScat Ku-BAND RADAR > RapidScat Ku-Band Radar" ;
:instrument_vocabulary = "RapidScat Ku-BAND RADAR > RapidScat Ku-Band Radar" ;
:time_coverage_resolution = "P1d" ;
:geospatial_lat_min = -67.057541 ;
:geospatial_lat_max = 67.057541 ;
:geospatial_lon_min = -180. ;
:geospatial_lon_max = 180. ;
:geospatial_x_units = "meters" ;
:geospatial_y_units = "meters" ;
:naming_authority = "org.doi.dx" ;
:date_created = "2026-01-16T20:22:06GMT" ;
:date_modified = "2026-01-16T20:22:06GMT" ;
:date_issued = "2026-01-16T20:22:06GMT" ;
:date_metadata_modified = "2026-01-16T20:22:06GMT" ;
:input_data_quality_filtering = "Only used highest-quality input data." ;
:acknowledgement = "This data set was created in part with funding from NASA Grant #80
:processing_level = "Level 3" ;
:creator_name = "David Long" ;
:creator_type = "person" ;
:creator_email = "long@ee.byu.edu" ;
:creator_url = "http://www.scp.byu.edu" ;
:creator_institution = "Electrical and Computer Engineering Department\nBrigham Young
:geospatial_bounds = "POLYGON((-67.057541 -180.000000, -67.057541 180.000000, 67.05754
:geospatial_bounds_crs = "EPSG:6933" ;
:geospatial_lat_units = "degrees_north" ;
:geospatial_lon_units = "degrees_east" ;
:geospatial_x_resolution = "3128.16 meters" ;
```

```
:geospatial_y_resolution = "3128.16 meters" ;
:time_coverage_start = "2016-06-30T23:59:00.00Z" ;
:time_coverage_end = "2016-07-01T23:56:07.62Z" ;
:time_coverage_duration = "P00T23:57:00.12" ;
:number_of_input_files = 47 ;
:input_file1 = "RS_S1B10067.20180201232.h5" ;
:input_file2 = "RS_S1B10068.20180201232.h5" ;
:input_file3 = "RS_S1B10069.20180201232.h5" ;
:input_file4 = "RS_S1B10070.20180201232.h5" ;
:input_file5 = "RS_S1B10071.20180201233.h5" ;
:input_file6 = "RS_S1B10072.20180201233.h5" ;
:input_file7 = "RS_S1B10073.20180201233.h5" ;
:input_file8 = "RS_S1B10074.20180201235.h5" ;
:input_file9 = "RS_S1B10075.20180201235.h5" ;
:input_file10 = "RS_S1B10076.20180201235.h5" ;
:input_file11 = "RS_S1B10077.20180201236.h5" ;
:input_file12 = "RS_S1B10078.20180201237.h5" ;
:input_file13 = "RS_S1B10079.20180201237.h5" ;
:input_file14 = "RS_S1B10080.20180201237.h5" ;
:input_file15 = "RS_S1B10081.20180201238.h5" ;
:input_file16 = "RS_S1B10082.20180201244.h5" ;
:input_file17 = "RS_S1B10083.20180201245.h5" ;
:input_file18 = "RS_S1B10084.20180201245.h5" ;
:input_file19 = "RS_S1B10085.20180201246.h5" ;
:input_file20 = "RS_S1B10086.20180201246.h5" ;
:input_file21 = "RS_S1B10092.20180201249.h5" ;
:input_file22 = "RS_S1B10093.20180201249.h5" ;
:input_file23 = "RS_S1B10094.20180201250.h5" ;
:input_file24 = "RS_S1B10095.20180201250.h5" ;
:input_file25 = "RS_S1B10096.20180201250.h5" ;
:input_file26 = "RS_S1B10097.20180201250.h5" ;
:input_file27 = "RS_S1B10098.20180201251.h5" ;
:input_file28 = "RS_S1B10099.20180201257.h5" ;
:input_file29 = "RS_S1B10100.20180201258.h5" ;
:input_file30 = "RS_S1B10101.20180201258.h5" ;
:input_file31 = "RS_S1B10102.20180201258.h5" ;
:input_file32 = "RS_S1B10103.20180201258.h5" ;
:input_file33 = "RS_S1B10104.20180201259.h5" ;
:input_file34 = "RS_S1B10105.20180201259.h5" ;
:input_file35 = "RS_S1B10106.20180201300.h5" ;
```

```
  :input_file36 = "RS_S1B10107.20180201300.h5" ;
  :input_file37 = "RS_S1B10108.20180201301.h5" ;
  :input_file38 = "RS_S1B10109.20180201301.h5" ;
  :input_file39 = "RS_S1B10110.20180201301.h5" ;
  :input_file40 = "RS_S1B10111.20180201307.h5" ;
  :input_file41 = "RS_S1B10112.20180201309.h5" ;
  :input_file42 = "RS_S1B10113.20180201310.h5" ;
  :input_file43 = "RS_S1B10114.20180201310.h5" ;
  :input_file44 = "RS_S1B10115.20180201310.h5" ;
  :input_file45 = "RS_S1B10116.20180201311.h5" ;
  :input_file46 = "RS_S1B10117.20180201311.h5" ;
  :input_file47 = "RS_S1B10118.20180201311.h5" ;
}
```